A Comparison of Two Numerical Methods for Integrating a Quasi-geostrophic Multilayer Model of Ocean Circulations: Finite Element and Finite Difference Methods

CHRISTIAN LE PROVOST, CHRISTINE BERNIER,* AND ERIC BLAYO

Laboratoire des Ecoulements Géophysiques et Industriels, Institut de Mécanique de Grenoble, BP 53X, 38041 Grenoble Cedex, France

To study the feasibility of using the finite elements method for ocean modelling, a quasi-geostrophic eddy resolving general circulation model has been driven, using either a classical finite differences technique or a finite elements technique. This feasibility has been clearly demonstrated, and a comparison of the models' performances shows that, for simulations of realistic basins, the finite elements model CPU cost is only four times the finite difference model cost. © 1994 Academic Press, Inc.

1. INTRODUCTION

Ocean circulation numerical modelling started in the sixties with Sarkisyan [43] and Bryan and Cox [11]. Since then, tremendous progress has been made in this field, thanks to a better understanding of the ocean dynamics and thermodynamics, improvements in the physics included in the models, the development of new modelling techniques, and the spectacular improvement in the performance of computers. The aim of this paper is to contribute to one of these domains by examining the possible use of one numerical technique which has until now not really been applied to ocean numerical modelling: the finite element technique. It would be beyond the scope of this paper to give an extensive description of the progress and achievements made in the field over the last few years with the more traditional finite difference techniques. However, in order to better understand the context of the following developments and to provide the reader with benchmarks for the present study, within the huge and very complex field of ocean numerical modelling, it is important to address some related issues in this Introduction: primitive equation (PE) versus more simplified models, eddy resolving versus noneddy resolving models, various vertical descriptions of the domain studied

and its vertical discretization, and, finally, horizontal discretization.

The ocean is a tridimensional domain. Basically, the Navier Stokes equations and equations for the conservation of heat and salt allow us to describe the dynamics and thermodynamics of the ocean. However, the horizontal scales of the world ocean are much larger than the vertical scale, and the compressibility of sea water is weak. This makes it possible to reduce the Navier Stokes equations under two major assumptions (hydrostatic balance and Boussinesq approximations), leading to the so-called primitive equation formulation (PE model) [12]. The early models were based on this PE formulation: Friedrich [21] for the North Atlantic, Cox [15] for the Indian Ocean, and Bryan, Manabe, and Pacanowski [13] for world ocean circulations. Despite their coarse vertical and horizontal resolutions, they were able to produce current and water mass characteristics which qualitatively compared reasonably well with observations. However, these models were obviously too viscous, because of their lack of resolution and the crude parameterization of the subgrid scale processes. Hence the efforts in the field of ocean modelling started with Holland and Lin [26], to investigate the role of mesoscale eddy motions in global circulations, by explicitly resolving these scales in the simulations. These models were called EGCMs (eddy general circulation models) in contrast to the GCMs (general circulation models) mentioned above. These EGCMs need a very high resolution: their mesh must correspond to at least a fraction of the first internal radius of deformation, of the order of 40 km at midlatitudes. Because of computer limitations, these investigations were mainly carried out on simpler models than the PE models. The ocean dynamics is strongly geostrophic, due to the scales of the flows and the rotation of the earth, and this allows the development of simpler models: quasi-geostrophic (QG) models [27] and balance equation models [22], among others. These models are

* Laboratoire de Modélisation et Calcul, Institut de Mathématiques Appliquées de Grenoble, BP 53X, 38041 Grenoble Cedex, France

much cheaper in terms of computer time, and their output is easier to understand than the more complex output of the PE models. Hence the possibility provided by the computers of the eighties to carry out very high resolution experiments, with meshes of the order of 10 km [1]. These studies, developed over more than 15 years, have led to a comprehensive understanding of the processes controlling the mean and eddy kinetic and potential energy distributions over large parts of the world ocean. Nevertheless, it must be acknowledged that it is still not known how to properly parameterize these small-scale Reynold stresses in large-scale coarse resolution models, where the mesoscales are not explicitly and correctly resolved. Hence the current tendency to take advantage of rapidly increasing computer power and develop high resolution realistic numerical models. However, they are still limited, because of limitations on the largest scientific computers now available, to half a degree resolution for global ocean scales [45], or to $\frac{1}{3}$ to $\frac{1}{6}$ of a degree for basin scale experiments: Bryan and Holland [10] and Böning *et al.* [9] for the North Atlantic, and Webb *et al.* [48] for the Antarctic circumpolar current. There is thus a strong demand for new models which can be used to focus and increase the horizontal resolution over special areas of major importance, without exceeding the present computer limits. The finite element technique can offer such a possibility. However, it has never been tested in ocean circulation modelling. The aim of this paper is precisely to contribute to the promotion of this method. In order to start with a simplified context, and reasonable computer costs, we have decided to limit our investigations first to a QG experiment in an EGCM mode.

Another major issue in ocean modelling is the way in which the vertical structure of the domain is described and its discretisation is treated. The ocean is vertically stratified, with quasi-horizontal isopycnics (i.e., levels of same density), except within fronts. Hence one class of ocean models approximating the vertical density structure with layers of constant density: the simpler two-layer models have thus immensely contributed to explaining many ocean circulation phenomena (see, for example, [39, 44]). Another approach, which retains the continuously stratified nature of the ocean, is to separate the vertical structure from the time and horizontal structure in the equations of motion; this approach was first restricted to the inviscid equations linearized about a static background density for a flat bottom ocean, thus allowing analytical approaches to be used [33, 41]. These are the so-called modal equations, each mode satisfying a set of shallow water type equations. The inclusion of the vertical mixing of heat and momentum has been demonstrated to be possible by McCreary [34], while the inclusion of topography with nonlinear and diffusion terms has been considered by Flierl [20], Davies [17], van Forest and Brundrit [47]. However, this approach becomes inefficient if many modes and their interactions have to be

considered. The alternative is to replace the vertical coordinate z by a generalized vertical coordinate s, a function of space, time, and some characteristic physical parameter of the problem [29]. The more classical level model can be considered as part of this classification, by taking $s = z$. Choosing $s = p$, pressure, is very popular in meteorology, but rarely used for complex realistic applications because the lower boundary conditions are awkward. Taking $s = \rho$, density (or potential density), leads to the isentropic coordinates: the rationale for this choice is that, in the interior of the ocean, density of a particle is nearly conserved because of the absence of strong mixing processes, the flows being along isopycnals. The above mentioned layer-models are simplified versions of this formulation. The development of the isopycnic coordinates for realistic ocean circulation models has encountered technical difficulties related to the fact that isopycnals can intersect boundaries (sea surface, or topography). The treatment of turbulent processes due to mixed layer dynamics near the surface is another major problem. This approach has been intensively investigated by Bleck and Boudra [5], Oberhuber [38], and Bleck *et al.* [6] and is now under test in basin-scale ocean circulation experiments [36] and in global ocean scale experiments [38]. Another generalized vertical coordinate system is the so-called "sigma system," which attempts to simplify computations at the top and bottom boundaries by taking, for example, $s = z/D$, where D is the local depth of the ocean; this approach is well adapted to follow complex bottom topography; however, serious problems related to truncation errors have to be circumvented when there are abrupt changes in topography (see, for example, [7, 25]. As stated before, our goal in this paper is to investigate the possibilities of the finite element technique as a way of obtaining greater flexibility to deal with the horizontal resolution of ocean circulation problems. Thus, in the following paragraphs, we have decided to treat the vertical dimension using the simpler layer formulation, as a straightforward extension of the two-layer formulation described by Holland [27].

As many of the above mentioned approaches, the N-layer QG formulation that is presented in Section 2 as the baseline system on which our tests are carried out, results in the solution of a system of elliptic partial differential equations. A large variety of methods have been developed for the numerical solution of such systems [3]: finite difference, finite elements, and spectral methods have all been employed with success. Finite difference methods (FDMs) replace the continuous differential equations with discrete difference equations. Finite element methods (FEMs) reformulate the differential equations as a variational principle. The spectral methods expand the unknown solutions in terms of predetermined basis sets and employ orthogonality relations. The finite difference methods are the simplest to program and have thus been the most common used in

ocean modelling. Spectral methods have been intensively used for process studies in simplified basin geometries, like biperiodic domains and zonal channels, because of their advantages over finite difference methods in terms of accuracy for a given number of independent degrees of freedom. For ocean modelling, FEMs were first applied in the area of higher frequency phenomena, like tides: Grotkop [3], Connor and Wang [14], Taylor and Davies [46], for example, presented ways for solving the shallow water equations with that technique, and since then this approach has been intensively developed for coastal dynamics [49] and global ocean tide modelling [31]. The feasibility and utility of FEMs for modelling ocean dynamics was addressed for the first time by Fix [19] who investigated their properties within the simplifying quasi-geostrophic approximation. He concluded that there were several advantages: precision, conservation of energy and enstrophy, natural treatment of boundary conditions, flexibility of discretisation for complex areas. He demonstrated the stability and convergence of the semi-discrete finite element formulation of the problem and established the conservative properties of its numerical approximation for energy, vorticity, and enstrophy, independently of the irregularity of the grid used for spatial integration. Given these conclusions, some attempts were made to introduce FEMs in the field of ocean modelling. Haidvogel, Robinson, and Schulman [24] compared the precision of a finite difference model, a finite element model, and a spectral model, for applications to open ocean problems and concluded that it would be of value to develop the FEM. Dumas, Le Provost, and Poncet [18] investigated the performances of an FE model in solving the classical barotropic wind-driven mid-latitude ocean basin circulation problem and found that the precision of their results compared favorably with the analytical solutions of Stommel and Munk for linear cases and with the earlier results obtained by FD techniques for non-linear cases. As their solutions typically include a western boundary layer with intense velocity gradients, the advantage of refining the triangulation along the western wall of the basin was clearly illustrated. These early models were then extended to the more realistic case of vertically stratified domains: Miller, Robinson, and Haidvogel [35] developed methods to deal with the depth dependence of the flow, keeping a FE method on the horizontal, and testing a collocation method on the vertical. The model was then intensively applied to realistic open ocean modelling problems (see, for instance, [42]). Le Provost [30] applied an extension of the barotropic finite difference model of Dumas et al. to a two-layer stratified domain, but the advent of vector computers at about the same time slowed down efforts in that direction because of the very high performance level on this class of computer of the more classical finite difference models based on fast Fourier cyclic reduction methods.

The aim of this paper is to take another look at this extension of the FE method to a multilayer ocean, because of the renewed interest in the field of ocean modelling, in testing alternative techniques to the standard FD codes, as stated above. As stated earlier, the paper will be limited to the quasi-geostrophic formulation for the sake of simplicity, but the method for solving the associated Helmholtz equations is valid for the more general case of the so-called PE models generally used for realistic ocean circulation modelling simulations. The first part will review the general formulation of the QG stratified ocean circulation model equations. The second part will present the method used to numerically solve these equations over a closed domain, using a leapfrog method for time dependence and either a classical FFT cyclic reduction FD method or a new FE method for space integration at every time step. The third part presents the physical features of a numerical solution chosen as a test. In the fourth part, the performances of the two methods will be compared in terms of quantitative numerical output and computer costs. Finally, the results will be generalized to more realistic situations for practical applications to real ocean basins, and the conclusions will be extended to more complete primitive equation numerical ocean modelling.

2. OCEAN CIRCULATION MODEL: QUASI-GEOSTROPHIC FORMULATION

Equations

The ocean is vertically stratified in terms of temperature, salinity, and density. In the present quasigeostrophic formulation, only density stratification is considered. The vertical structure is modelled by dividing the domain into N layers ($i = 1$ to N) of density ρ_i and depth thickness at rest H_i. The governing equations are the quasi-geostrophic non-linear potential vorticity equations for each layer,

$$\frac{\partial}{\partial t} \nabla^2 \psi_i = J(\nabla^2 \psi_i + f, \psi_i) + \frac{f_0}{H_i}(w_{i-1/2} - w_{i+1/2})$$

$$- A\nabla^4 \psi_i - \delta_{iN}\varepsilon\nabla^2\psi_i + \delta_{i1}\frac{1}{H_1}\text{curl } \tau,$$

$$i = 1, ..., N \text{ layers;}$$

$$\delta_{ij} = 1 \quad \text{for} \quad i = j; 0 \quad \text{for} \quad i \neq j, \quad (1a)$$

coupled with the continuity equation applied at each interface,

$$\frac{\partial}{\partial t}(\psi_{i+1} - \psi_i) = J(\psi_{i+1} - \psi_i, \psi_{i+1/2}) + \frac{g^{i+1/2}}{f_0}w_{i+1/2},$$

$$i = 1, ..., N-1 \text{ interfaces.} \quad (1b)$$

ψ_i are the quasi-geostrophic stream functions in the various layers, and $w_{i+1/2}$ is the vertical velocity at the interface $i+1/2$. According to the formula used by Phillips [40], the interfacial stream function $\psi_{i+1/2}$ is evaluated as the weighted average of ψ_{i+1} and ψ_i:

$$\psi_{i+1/2} = \frac{H_{i+1}\psi_i + H_i\psi_{i+1}}{H_i + H_{i+1}}.$$

The velocity components for each layer are $u_i = -\partial\psi_i/\partial y$ and $v_i = \partial\psi_i/\partial x$. Equations (1a) expresses that the local rate of change of relative vorticity in each layer is produced by horizontal advection, stretching of the water columns, dissipative harmonic friction with coefficient A, bottom frictional effects on the lower layer with coefficient ε, and vorticity input by the wind stress curl in the upper layer. Equation (1b) can be considered as predicting the deviation $h_{i+1/2}$ of each interface from its equilibrium position $(h_{i+1/2} = -f_0(\psi_{i+1} - \psi_i)/g^{i+1/2})$, with $g^{i+1/2}$ being the reduced gravity $g^{i+1/2} = g(\rho_i - \rho_{i+1})/\rho_0$, where ρ_0 is the mean density over the whole domain. J is the jacobian operator; $f = f_0 + \beta(y - y_0)$ is the variable coriolis parameter (y_0 refers to the mid-latitude of the basin).

Boundary Conditions

For practical tests, and within the scope of this paper, Eqs. (1) are integrated over a very simplified domain Ω: a square box of constant depth. The forcing will be a wind stress curl of intensity τ_0, zonally constant and meridionally sinusoïdal, inducing a two-gyre ocean circulation pattern. Such an academic case has been intensively investigated over the last 10 years in an attempt to study the role of inertia and mesoscale eddies in the subtropical and subpolar gyre circulations at midlatitudes.

In this formulation, streamfunctions in each layer must take constant values at each time step along the side walls $\partial\Omega$ of the domain:

$$\psi_i = C_i(t) \qquad \text{on } \partial\Omega \qquad \text{for } i = 1, ..., N.$$

These $C_i(t)$ have to be computed at each time step, for each layer, in order to conserve mass:

$$\int_\Omega w_{i+1/2}\, dx\, dy = 0;$$

i.e.

$$\int_\Omega \frac{\partial}{\partial t}(\psi_{i+1} - \psi_i)\, dx\, dy = 0 \Rightarrow \int_\Omega (\psi_{i+1}(t) - \psi_i(t))\, dx\, dy$$

$$= \int_\Omega (\psi_{i+1}(t=0) - \psi_i(t=0))\, dx\, dy.$$

A complementary boundary condition is necessary along $\partial\Omega$, because the problem to be solved corresponds to a second-order Helmholtz type equation: the vorticity $\xi_i = \nabla^2\psi_i$ will be prescribed. For the present tests, $\xi_i = 0$ (slip condition) will be chosen.

Matricial Formulation

In order to simplify the writing of the following, it is useful to introduce a matricial formulation. By eliminating $w_{i+1/2}$ from system (1) and using the notations,

$$\Psi = (\psi_1, ..., \psi_N)^T$$

$$W = \begin{pmatrix} R_1' & -R_1' & 0 & & \\ -R_2 & R_2 + R_2' & -R_2' & 0 & \\ 0 & -R_3 & R_3 + R_3' & -R_3' & 0 \\ & & & & -R_N R_N \end{pmatrix}$$

with

$$R_i' = \frac{f_0^2}{g^{i+1/2}H_i} \qquad \text{and} \qquad R_{i+1} = \frac{f_0^2}{g^{i+1/2}H_{i+1}},$$

system (1) can be written

$$\frac{\partial\Theta}{\partial t} = E + A(\nabla^2\Theta + W\Theta + W^2\Psi) + D \qquad (2a)$$

$$\Theta = \nabla^2\Psi - W\Psi \qquad \text{in } \Omega \qquad (2b)$$

with

$$E = \begin{pmatrix} J(\theta_1 + f, \psi_1) \\ J(\theta_2 + f, \psi_2) \\ \vdots \\ J(\theta_N + f, \psi_N) \end{pmatrix} \qquad \text{and} \qquad D = \begin{pmatrix} 1/H_1\, \text{curl}\, \tau \\ 0 \\ \vdots \\ -\varepsilon\nabla^2\psi_N \end{pmatrix}.$$

The existence and unicity of the solution for problem (2) with the above boundary conditions was proved by Bernier [2].

Formulation through Eigen Modes

The difficulty in solving (2) is that, given the tridiagonal structure of matrix W, the problem is fully implicit, with links between layers $i-1$, i, and $i+1$, and that Eqs. (2a) and (2b) are coupled. It is possible to decouple the resolution of Eqs. (2) on the vertical by looking at solutions in terms of modes in the base which diagonalizes matrix W.

Let B be the matrix required to switch from a layer formulation to a mode formulation of the problem, and $\Lambda = B^{-1}WB$. Λ is the diagonal matrix of the eigenvalues λ_k of W. The elements of matrix B are denoted (b_{ij}),

$i, j = 1 \cdots N$, and those of $B^{-1} : b_{ij}^{-1}$. Also, we use $(*)$ for the eigenvector solutions:

$$\Psi = B\Psi^* \qquad \text{and} \qquad \Theta = B\Theta^*.$$

Matrix B is normalized so that

$$\frac{1}{H} = \sum_{i,j=1}^{N} \frac{(b_{ij}^{-1})^2}{H_i}, \qquad \sum_{j=1}^{N} b_{1j}^{-1} = 1,$$

$$\sum_{j=1}^{N} b_{ij}^{-1} = 0 \qquad \text{for} \quad i \neq 1.$$

N.B. The first eigenvalue of W is zero.

After multiplication by B^{-1}, system (2) becomes

$$\frac{\partial \Theta^*}{\partial t} = B^{-1}E + A(\nabla^2 \Theta^* + A\Theta^* + A^2 \Psi^*) + B^{-1}D \qquad (3a)$$

$$\Theta^* = \nabla^2 \Psi^* - A\Psi^* \qquad \text{in } \Omega. \qquad (3b)$$

Adimensionalisation

Before proceeding further, let us adimensionalise Eq. (3). We take the following order of magnitudes for the main variables and functions in relation to the characteristics of the physical problem addressed:

L, horizontal scale of the domain Ω,

U, horizontal velocity scale;

$T = (\beta_0 L)^{-1}$ time scale, where β_0 is the meridional gradient of the Coriolis parameter, at the median latitude of the basin;

τ_0, wind stress scale.

This adimensionalisation results in a definition of typical scales associated with the major processes controling the solution (see, for example, Le Provost and Verron [32] for more details):

$\delta_v^3 = A/(\beta_0 L^3)$, width of the lateral friction boundary layer;

$\delta_f = \varepsilon/(\beta_0 L)$, width of the bottom friction boundary layer;

$\delta_i^2 = U/(\beta_0 L^2)$, width of the inertial boundary layer;

$A' = L^2 A$, adimensional eigenvalue matrix.

In the following, all the variables are adimensional. The equations are then

$$\frac{\partial \Theta^*}{\partial t} = B^{-1}E + \delta_v^3(\nabla^2 \Theta^* + A'\Theta^* + A'^2 \Psi^*) + B^{-1}D \qquad (4a)$$

$$\Theta^* = \nabla^2 \Psi^* - A'\Psi^* \qquad \text{in } \Omega \qquad (4b)$$

with

$$E = \begin{pmatrix} J(\delta_i^2 \theta_1 + y, \psi_1) \\ J(\delta_i^2 \theta_2 + y, \psi_2) \\ \vdots \\ J(\delta_i^2 \theta_N + y, \psi_N) \end{pmatrix} \qquad \text{and} \qquad D = \begin{pmatrix} 1/H_1 \, \text{curl} \, \tau \\ 0 \\ \vdots \\ -\delta_f \nabla^2 \psi_N \end{pmatrix}$$

with the boundary conditions:

$$\nabla^2 \psi_i = 0 \qquad \text{on } \partial\Omega \quad \text{for} \quad i = 1 \cdots N$$

$$\psi_i = C_i(t) \qquad \text{on } \Omega \quad \text{for} \quad i = 1 \cdots N$$

$$\int_\Omega w_{i+1/2} \, dx \, dy = 0.$$

Method for time integration

We thus have to integrate Eqs. (4) with the above boundary conditions in space and time. The classical leapfrog method with three time step levels is used for the time integration. The non-linear and Coriolis terms are taken at the intermediate time step n. With regard to the frictional terms, the term corresponding to the studied mode is isolated from the others and treated semi-explicitly. We thus have

$$\frac{\Theta^{*,n+1} - \Theta^{*,n-1}}{2\Delta t} = B^{-1}E^n + \delta_v^3 \{(\nabla^2 \Theta^{*,n+1} + \nabla^2 \Theta^{*,n-1})/2$$

$$+ A'\Theta^{*,n} + A'^2 \Psi^{*,n}\}$$

$$+ S - \delta_f \{BB[(\Theta^{*,n+1} - \Theta^{*,n-1})/2$$

$$+ A'\Psi^{*,n}] + TC^n\} \qquad (5a)$$

$$\Theta^{*,n+1} = \nabla^2 \Psi^{*,n+1} - A'\Psi^{*,n+1} \qquad \text{in } \Omega \qquad (5b)$$

with $BB = $ diagonal matrix of diagonal elements $(b_{i,N}^{-1} b_{N,i})$ and

$$TC = \begin{pmatrix} b_{1N}^{-1} \sum_{j \neq 1} b_{Nj}(\theta_j^* + \lambda_j \psi_j^*) \\ b_{2N}^{-1} \sum_{j \neq 2} b_{Nj}(\theta_j^* + \lambda_j \psi_j^*) \\ \vdots \\ b_{NN}^{-1} \sum_{j \neq N} b_{Nj}(\theta_j^* + \lambda_j \psi_j^*) \end{pmatrix}$$

and

$$S = \begin{pmatrix} 1/H_1 \, \text{curl} \, \tau \\ 0 \\ \vdots \\ 0 \end{pmatrix};$$

i.e.,

$$M\Theta^{*,n+1}$$

$$= F(\Theta^{*,n-1}, \nabla^2 \Theta^{*,n-1}, \Theta^{*,n}, \Psi^{*,n}, E^n, S, TC^n) \qquad (6a)$$

$$\nabla^2 \Psi^{*,n+1} - A'\Psi^{*,n+1} = \Phi^{*,n+1}, \qquad (6b)$$

where M is a diagonal matrix independent of time t, of diagonal element:

$$\frac{1}{2}\left(\frac{1}{\Delta t} + \delta_f(b_{iN}^{-1} b_{Ni}) - \delta_v^3 \nabla^2\right).$$

In order to satisfy the boundary conditions, auxilliary functions $\psi_{i,a}^*$, $\psi_{i,b}^*$, $\theta_{i,a}^*$, and $\theta_{i,b}^*$ are introduced:

$$\psi_i^* = \psi_{i,a}^* + C_i^*(t)\psi_{i,b}^* \qquad \theta_i^* = \theta_{i,a}^* - \lambda_i C_i^*(t)\theta_{i,b}^*$$

$$\psi_{i,a}^* = 0 \quad \text{on } \partial\Omega \qquad \theta_{i,a}^* = 0 \quad \text{on } \partial\Omega \qquad (7a),(7b)$$

$$\psi_{i,b}^* = 1 \quad \text{on } \partial\Omega; \qquad \theta_{i,b}^* = 1 \quad \text{on } \partial\Omega.$$

Functions $\psi_{i,b}^*$ and $\theta_{i,b}^*$ are independent of t and are calculated as follows:

$$M\Theta_b^* = 0 \quad \text{in } \Omega \qquad \nabla^2\psi_{i,b}^* - \lambda_i\psi_{i,b}^* = \theta_{i,b}^* \quad \text{in } \Omega$$

$$\Theta_b^* = 1 \quad \text{on } \partial\Omega; \qquad\qquad \psi_{i,b}^* = 1 \quad \text{on } \partial\Omega.$$

$$(8a), (8b)$$

$\theta_{i,a}^*$ and $\psi_{i,a}^*$ are then obtained as

$$M\Theta_a^{*,n+1} = F(\Theta^{*,n-1}, \nabla^2\Theta^{*,n-1},$$

$$\Theta^{*,n}, \Psi^{*,n}, E^n, S, TC^n)$$

$$\Theta_a^{*,n+1} = 0 \quad \text{on } \partial\Omega$$

$$\nabla^2\Psi_a^{*,n+1} - \Lambda'\Psi_a^{*,n+1} = \Theta_a^{*,n+1} \qquad (9)$$

$$\Psi_a^{*,n+1} = 0 \quad \text{on } \partial\Omega.$$

At $t = 0$, $\psi_i^0 = 0$. At each time step, system (9) must be solved. Constants $C_i^*(t)$ are then given by

$$\sum_\Omega \Psi_{i,a}^*(t) + C_i^*(t)\int_\Omega \Psi_{i,b}^* = 0,$$

thus making it possible to compute the complete solution at time t. The stability of this scheme was studied by Bernier [2].

In the following paragraphs, we will compare the performance of two methods for integrating system (9) within an oceanographic context, bearing in mind that, among other constraints, domain Ω generally has a complex geometry. These two methods are:

• a finite difference FFT cyclic reduction method, combined with a capacitance matrix method (not described here, but dealt with by Blayo and Le Provost [4]).

• a finite element method. To implement this method, a variational formulation must be determined.

Variational Formulation

We use the notations: $\{a, a'\} = \iint_\Omega a \cdot a' \, dx \, dy$ and the Green formula: $\{\nabla^2 a, a'\} = -\{\nabla a, \nabla a'\} + \int_{\partial\Omega} (\partial a/\partial n) \cdot a' \, ds$, where n is the normal direction to the boundary $\partial\Omega$ and s is a curvilinear coordinate along $\partial\Omega$.

Let us multiply Eqs. (9) by a test function Φ and integrate over the whole domain. Using the Green formula and given the fact that the curvilinear integrals along $\partial\Omega$ vanish (because $\Theta_a^{*,n+1}$ and $\Psi_a^{*,n+1}$ vanish along $\partial\Omega$), the problem can then be stated as: Find $\Theta_a^{*,n+1}$ and $\Psi_a^{*,n+1}$ in $(H_0^1(\Omega))^N$ so that $\forall\Phi \in (H_0^1(\Omega))^N$ $(H_0^1(\Omega) = $ Sobolev space),

$$\left[\frac{1}{2\Delta t}\text{Id} + \frac{\delta_f}{2}BB\right]\{\Theta_a^{*,n+1}, \Phi\} + \frac{\delta_v^3}{2}\{\nabla\Theta_a^{*,n+1}, \nabla\Phi\}$$

$$= \left[\frac{1}{2\Delta t}\text{Id} - \frac{\delta_f}{2}BB\right]\{\Theta_a^{*,n-1}, \Phi\}$$

$$+ \frac{\delta_v^3}{2}\{\nabla\Theta_a^{*,n-1}, \nabla\Phi\} + \{B^{-1}E^n, \Phi\}$$

$$+ \delta_v^3(\Lambda'\{\Theta^{*,n}, \Phi\} + \Lambda'^2\{\Psi^{*,n}, \Phi\})$$

$$\{S, \Phi\} - \delta_f[\{\Lambda'BB\Psi^{*,n}, \Phi\} + \{TC^n, \Phi\}]$$

and

$$\{\nabla\Psi_a^{*,n+1}, \nabla\Phi\} + \Lambda'\{\Psi_a^{*,n+1}, \Phi\}$$

$$= -\{\Theta_a^{*,n+1}, \Phi\} \quad \text{in } \Omega.$$

The computation of Θ_b^* and Ψ_b^* in $(H_0^1(\Omega))^N$ is carried out initially by solving the following variational problem, with $\Theta_b^{*,1}$ and $\Psi_b^{*,1}$ taken as unity along the boundary: Find $\Theta_b^{*,0}$ and $\Psi_b^{*,0}$ in $(H_0^1(\Omega))^N$ so that $\forall\Phi \in (H_0^1(\Omega))^N$,

$$\left[\frac{1}{2\Delta t}\text{Id} + \frac{\delta_f}{2}BB\right]\{\Theta_b^{*,0}, \Phi\} + \frac{\delta_v^3}{2}\{\nabla\Theta_b^{*,0}, \nabla\Phi\}$$

$$= \left[\frac{1}{2\Delta t}\text{Id} - \frac{\delta_f}{2}BB\right]\{\Theta_b^{*,1}, \Phi\} + \frac{\delta_v^3}{2}\{\nabla\Theta_b^{*,1}, \nabla\Phi\}$$

$$\Theta_b^* = \Theta_b^{*,0} + \Theta_b^{*,1}$$

$$\{\nabla\Psi_b^{*,0}, \nabla\Phi\} + \Lambda'\{\Psi_b^{*,0}, \Phi\}$$

$$= -\{\Theta_b^*, \Phi\} - \{\nabla\Psi_b^{*,1}, \nabla\Phi\} + \Lambda'\{\Psi_b^{*,1}, \Phi\}$$

$$\Psi_b^* = \Psi_b^{*,0} + \Psi_b^{*,1}.$$

Finite Element Formulation

If, with $m = 1$ to N modes or layers, we let:

$A_m = (a_i)_m$, the integration points of the domain

$K = \text{Card } A_m$

$p_i = $ test function of value one at the integration point a_i and zero elsewhere.

Then for each mode (or layer), the variables are expressed as linear combinations of the p_i functions:

$$\Psi_m^* = \sum_{i=1}^K p_i \Psi_{m,i}^*.$$

The matrices which must be used are linear combinations of two basic matrices:

$$\text{TMAS} = [\{p_i, p_j\}]_{i,j} \quad \text{and} \quad \text{TCOUR} = [\{\nabla p_i, \nabla p_j\}]_{i,j}.$$

These two matrices are symmetrical, definite positive, sparse, and not time-dependent. For the different layers, the corresponding matrices are

$$\text{TMAS}_m = \left[\frac{1}{2\Delta t}\text{Id} + \frac{\delta_f}{2} b_{m,N}^{-1} b_{N,m}\right]\text{TMAS} + \frac{\delta_v^3}{2}\text{TCOUR}$$

and

$$\text{TCOUR}_m = \text{TCOUR} + \lambda_m \text{TMAS}.$$

We thus have $2N$ matrices. In practice, after having built a finite element grid, the computations are made in the following sequence:

Initialisation:

- initialisation of the physical constants,
- computation of matrices A, BB, B, B^{-1},
- construction of the matrices TMAS and TCOUR, TMAS_m and TCOUR_m,
- beginning of computation of Θ_b^* and Ψ_b^*,
- Choleski decomposition of matrices TMAS_m and TCOUR_m,
- computation of right-hand source members,
- end of computation of Θ_b^* and Ψ_b^*
- computation of $\int_\Omega \Psi_{i,b}^*$;

For each time step:

- computation of the Jacobian and other source terms for the right members, by layers,
- switch from layers to modes,
- computation of the second member for the vorticity equations,
- resolution of the vorticity equations to obtain Θ_a^*,
- computation of the second member for the stream function equations,
- resolution of the streamfunction equations to obtain Ψ_a^*,

- computation of the boundary constants $C_m^*(t)$,
- computation of Θ^* and Ψ^*,
- switch back from modes to layers;

Comment:

The resolution of these linear systems must be very efficient. Two kinds of methods have been tested: direct and iterative. Given the fact that the matrices are symmetrical, we have taken the Choleski method as a direct method, and the preconditioned conjugate gradient as an iterative method. Tests were carried out on two 550×550 linear systems, corresponding to mass and stiffness matrices for P2 finite elements. Whatever the choice of preconditioning, the direct method was shown to be the fastest. The complete Choleski decomposition was made once, at the beginning of the resolution.

The computations of the right-hand sides of the equations to be solved need only linear combinations between matrices and vectors. Hence there is an efficient vectorization of the code on a Cray computer.

3. NUMERICAL TESTS

Choice of Numerical Parameters

In order to test this finite element model against the more classical, and very efficient, cyclic reduction FFT +
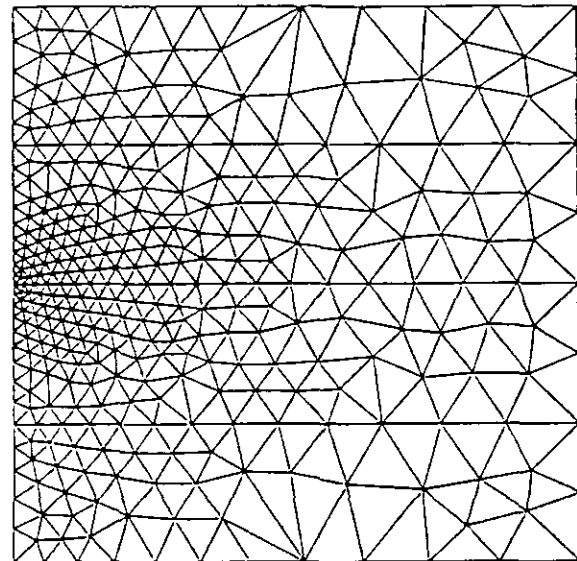

FIG. 1. Grid used for the finite element application. The characteristics of this grid are the following: 630 triangles, 345 gridpoints, 1319 degrees of freedom per layer. The half bandwidth of the associated matrix is 101 elements. If this domain corresponds to a square ocean of 2000 km × 2000 km, the resolution along the western boundaries is 18 km in the middle of the basin and 109 km on the eastern side. In comparison, the resolution for the uniform grid used for the finite difference application is 20 km everywhere, i.e. 10,201 degrees of freedom.

capacitance method, one standard kind of experiment was reproduced, an experiment which has already been used intensively in recent years to investigate the physical properties of eddy resolving general ocean circulation models (see, for example, [28] or, more recently, [1]). The numerical experiments were restricted to a rectangular domain, and controlling parameters were chosen in order to remain within a simple class of physical processes.

The size of the basin is limited to 2000 km × 2000 km, with a constant depth of 5000 m, located at a mid-latitude of 40° ($f_0 = 0.93 \times 10^{-4}$ s^{-1}, $\beta_0 = 2 \times 10^{-11}$ m^{-1}s^{-1}), and oriented so that the x direction is east and the y direction
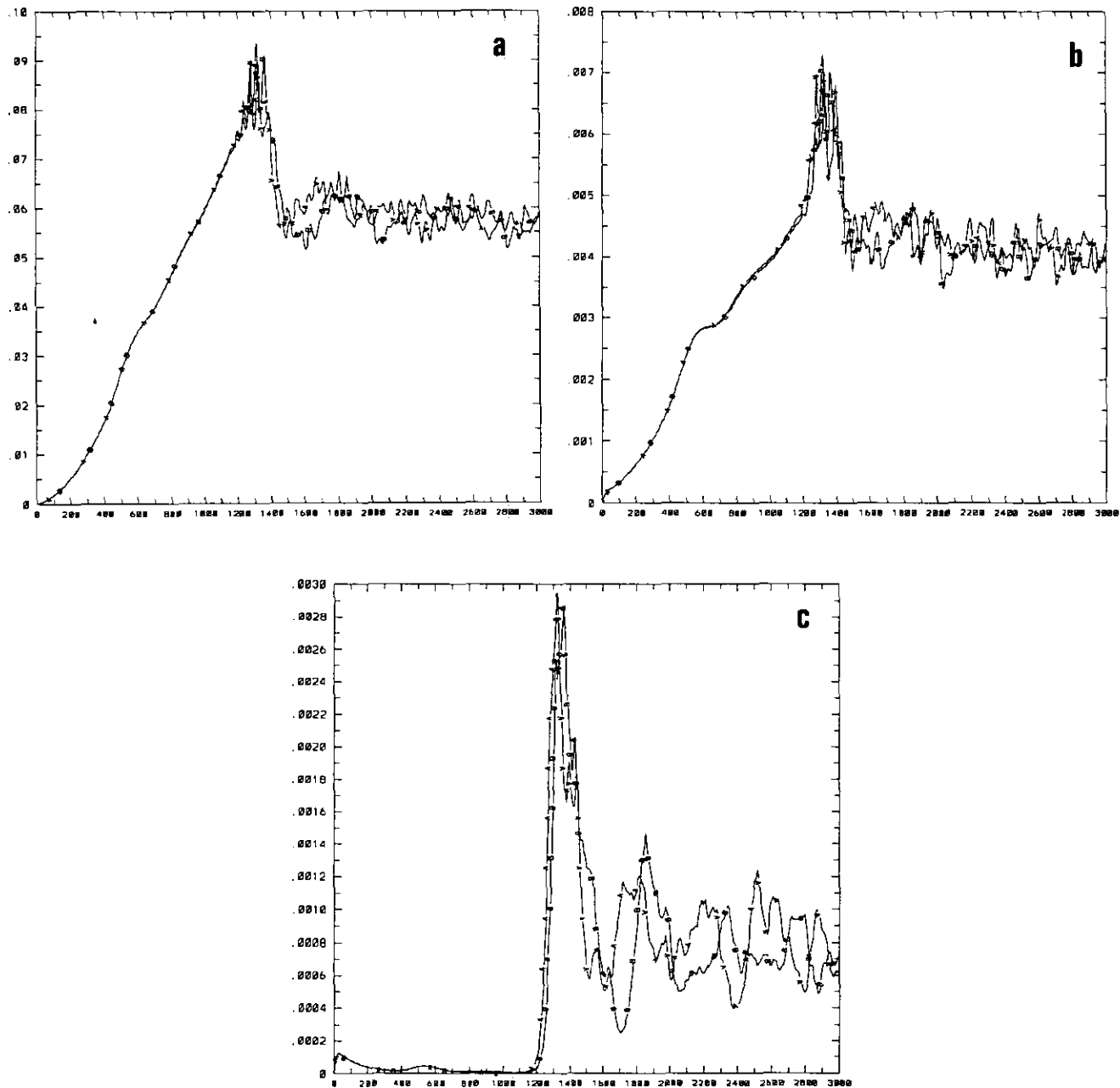
FIG. 2. Time history of the basin average kinetic energy for the finite element (A) and finite difference (B) solutions over the 3000 days of integration of the comparison test. Units are the same for the three layers: (a) 0.1 m^{2}s^{-2} full scale for layer 1; 0.08 m^{2}s^{-2} full scale for layer 2; and (c) 0.003 m^{2}s^{-2} full scale for layer 3. Note the different phases of the experiment: the linear spinup from days 0 to 600, the buildup of the inertial circulation (jet formation along the zero wind stress curl and eastward penetration, and westward recirculation) from day 600 to 1200, destabilization of flows and setting up of turbulent regime from day 1200 to 1400, and progressive establishment of the turbulent solution around its mean steady state from day 1400 to the end of the simulations.

north, with the origin of the cartesian tangent reference coordinate system at mid-latitude on the western solid boundary. The domain Ω is then $\{x \in [0, L]; y \in [-0.5L, +0.5L]\}$. The wind forcing pattern is taken as

$$\tau(x, y) = \tau_{max} \cos \frac{2\pi y}{L}; \quad \text{i.e.,} \quad \text{curl } \tau = -\frac{2\pi \tau_{max}}{L} \sin \frac{2\pi y}{L}.$$

It drives a double-gyre circulation within the basin, symmetrical in relation to the mid-latitude $y = 0$. The vertical structure of the ocean is described by a three-layer stratification, with respective thicknesses of $H_1 = 300$ m, $H_2 = 700$ m, and $H_3 = 4000$ m, and reduced gravity coefficients of $g^{1 + 1/2} = 0.0357$ ms^{-2} and $g^{2 + 1/2} = 0.0162$ ms^{-2}.

We know from the physics of the problem thus formulated that this double-gyre circulation will develop intense western boundary currents (WBC). The width of the WBC depends on the relative values of typical parameters:

$$\delta_f = \frac{\varepsilon}{\beta L}, \qquad \delta_i = \left(\frac{U}{\beta L^2}\right)^{1/2}, \qquad \delta_v = \left(\frac{A}{\beta L^3}\right)^{1/3},$$

where $U = 2\pi\tau_{max}/\beta L(H_1 + H_2) \delta_f$, δ_i, and δ_v correspond to typical widths of flows controlled respectively by bottom friction effects, inertial effects in surface layers 1 and 2 (i.e., above the main thermocline of the ocean at mid-latitudes), and by lateral friction.

A typical value for the characteristic time scale of bottom damping is of the order of 116 days ($\varepsilon = 10^{-7}$s^{-1}). This value was therefore kept for the test. A realistic value of the wind stress is $\tau_{max} = 10^{-4}$m^{-2}s^{-2}. Then, the estimated widths of the bottom friction and inertial WB layers are: $\delta_f \cdot L = 5$ km and $\delta_i \cdot L = 28$ km. We can then tune the frictional coefficient A to "control" simulation features. This problem has been intensively analysed, especially in the barotropic case, and has recently been re-examined by Böning [8] and Le Provost and Verron [32]. We know that, in the control parameter space, moving from frictional regimes to increasingly inertial regimes shifts the flow from stable to unstable states, with western boundary flows developing a jet which expands eastward from the coast at the zero wind stress curl latitude and penetrates the domain to a variable extent, depending on the inertial character of the regime considered. Westward return flows then develop on each side of this jet. These flows, if inertial enough, can develop shear barotropic and baroclinic instabilities, which lead to meanders, and eddies drifting westward to join the WBC. For the present test, we have chosen a regime which can be considered as marginally stable; i.e., the jet flowing eastward remains stable, and only the return flow on the two sides of the jet is unstable. This regime is controlled by lateral friction: with $A = 1000$ m^{2}s^{-2}, the estimated width of the WBC $\delta_v L = 37$ km. We selected this intermediate

case, between frictional and inertial controls, because the corresponding solution is particularly sensitive to the numerical noise of the computation.

Choice of Grids and Time Steps

Knowing that the chosen test will lead to a solution with a WBC and a mid-latitude jet width of the order of 40 km, the finite difference grid is taken as 20 km and the finite element grid as presented in Fig. 1, with this 20 km-resolution
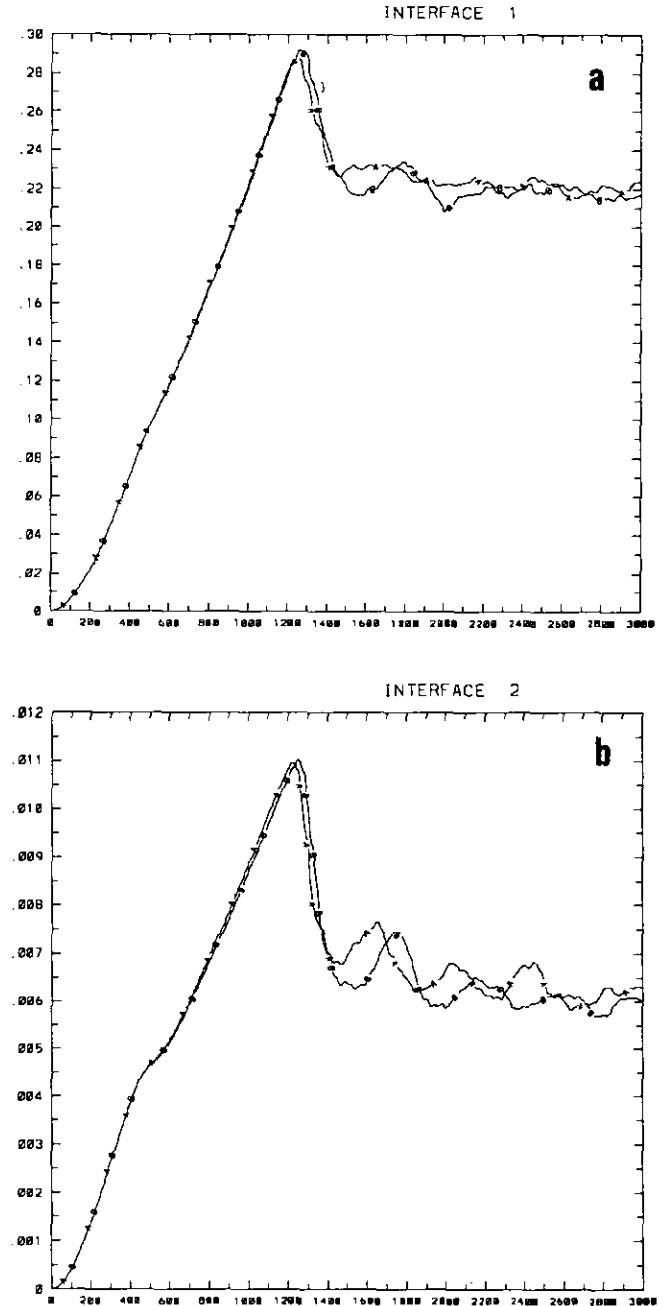

FIG. 3. The same as for Fig. 2, but for the basin average potential energy, (a) for interface $1 + \frac{1}{2}$ and (b) for interface $2 + \frac{1}{2}$.

in the western central part of the basin and a mesh increasing up to 100 km on the eastern boundary. The time step used for the FD model is typically 2 h a value chosen on the basis of experience. For the FE model, the experiment was started with the same 2 h ΔT, but it was necessary to decrease this time step to 1 h, in order to avoid numerical instabilities appearing when the turbulent regime developed.

Integral Energy Quantities for Global Control

Given the huge volume of information provided by the test experiments, one easy way to check the time evolution of the computed solutions is to integrate some energy quantities over the domain and for each layer. Kinetic and potential energy integrals were thus chosen:

$$K_i = \frac{H_i}{2} \int_\Omega |\nabla \psi_i|^2, \qquad \text{global kinetic energy of layer } i$$

$$P_{i+1/2} = \frac{f_0^2}{2g'_{i+1/2}} \int_\Omega |\tilde{\psi}_{i+1} - \tilde{\psi}_i|^2, \quad \text{where} \quad \tilde{\psi}_i = \psi_i - C_i,$$

global potential energy of interface $i + \frac{1}{2}$.

In the following experiments, these quantities will be plotted versus time and compared for each layer (Figs. 2a, b, c) and each interface (Figs. 3a, b).

4. BRIEF DESCRIPTION OF THE NUMERICAL EXPERIMENT CHOSEN FOR THE COMPARISON

The experiments are started from rest. Let us briefly review the different phases of the spinup (for more details, see, for example, Holland and Schmitz [28] or Le Provost and Verron [32]). At $t = 0$, the wind stress curl is applied to the surface of the basin, thus driving a flow in the upper layer which, by pressure effects, moves the lower layers and particularly the second layer which is above the main thermocline (see Figs. 2 and 3). Given the pattern of the wind stress curl, a double-gyre circulation results, which is symmetrical in relation to the zero wind stress curl line $y = 0$ (called the Sverdrup recirculations in this linear phase of the spinup). These flows accelerate and, because of the effect of the north–south gradient β of the Coriolis parameter $f = f_0 + \beta y$, they progressively build a western boundary current (WBC). This WBC becomes more and more energetic with time. It gradually results in a mid-basin zonal jet penetrating eastward along the zero wind stress curl line, and recirculating westward on the two sides through strongly inertial inner gyres superimposed on the Sverdrup global scale recirculation. This spinup needs a long integration: in Figs. 2 and 3, we can observe that the kinetic and potential energies increase regularly up to 1200 days. By this

time, a new phase develops which corresponds to the appearance of instabilities due to horizontal shears in the flows (barotropic instabilities) and vertical shears between the flows of the different layers (baroclinic instabilities). The barotropic instabilities are known to develop first in the westward recirculation section of the inner gyres [32]. Generally, they progressively destabilize the eastward jet itself, leading to meanders and eddy shedding. However, in the present case, the controlling parameters have been chosen so that the instabilities occur only in the westward recirculation and keep the jet stable. One advantage of this solution is precisely that it is very sensitive to the properties of the numerical schemes, which can lead, if these properties are poor, to artificial destabilization of the jet. These instabilities occur in the upper layers where the flow is very energetic. A major process which then takes place is the rapid transfer of energy to the lower layers, where the instabilities drive flows at the eddy scale (see period $t = 1200$–1600 days in Figs. 2 and 3). After a phase of adjustment, the whole dynamics of the basin reaches a quasi "steady state," where the global energy levels in the three layers stabilize, oscillating around mean typical values. The 3D flow is in statistical (and energetic) equilibrium: energy introduced in the basin by the wind field is now balanced by dissipation through lateral eddy viscosity in the different layers and bottom friction in the bottom layer.

Illustrations of typical instantaneous stream functions are shown for the three layers, at $t = 2000$ days in Fig. 4 and $t = 2500$ days in Fig. 5. In Figs. 4a and 5a, one may observe the strong and narrow jet penetrating eastward over $\frac{2}{3}$ of the width of the basin, the unstable westward return flow, and the western boundary currents. In Figs. 4b and 5b, for the second layer, the jet and the unstable inner gyre recirculation are still present, but the Sverdrup recirculations, at the basin scale, have almost completely disappeared, thus making it possible to clearly observe the presence of Rossby waves. These result from energy radiation, produced by the instabilities of the inner flows, and propagate westward. In Figs. 4c and 5c, for the bottom layer, only the signatures of the instabilities induced from the upper layers are visible, these being associated with eddies and Rossbly waves of layers 1 and 2. All these transient instabilities occur over time. The experiments were run until day 3000, as illustrated in figures 2 and 3, clearly showing that a statistical steady state was reached. From this set of instantaneous fields, mean flow solutions can be computed over a time sequence long enough to eliminate the unsteady part. The mean fields presented in figures 6 and 7 were obtained by averaging over 1000 days, from day 2000 to day 3000. Their main features may be summarised as follows: in figures 6a and 7a, based on FD and FE solutions, the mean stream function in the upper layer is characterized by a broad mid-basin jet, with return flows partly recirculating directly within a double inner gyre and the rest of the flow joining the large-scale

Sverdrup recirculation. In the second layer, the Sverdrup recirculation is virtually absent and the main flow is reduced to the double inner gyres on the two sides of the mid-basin jet. In the bottom layer, under the main thermocline, the mean flow exhibits a set of eight zonal gyres, alternatively cyclonic or anticyclonic, the strongest of which is under the mid-basin jet. These mean zonal gyres are typical of this class of experiment and physically related to the instabilities

of the upper layers and interfaces and to the eddy forcing which results (see, for example, [28]).

5. COMPARISON OF THE FD AND FE SOLUTIONS

This experiment was run with the two models, the main goal being to compare the performances of the two methods.
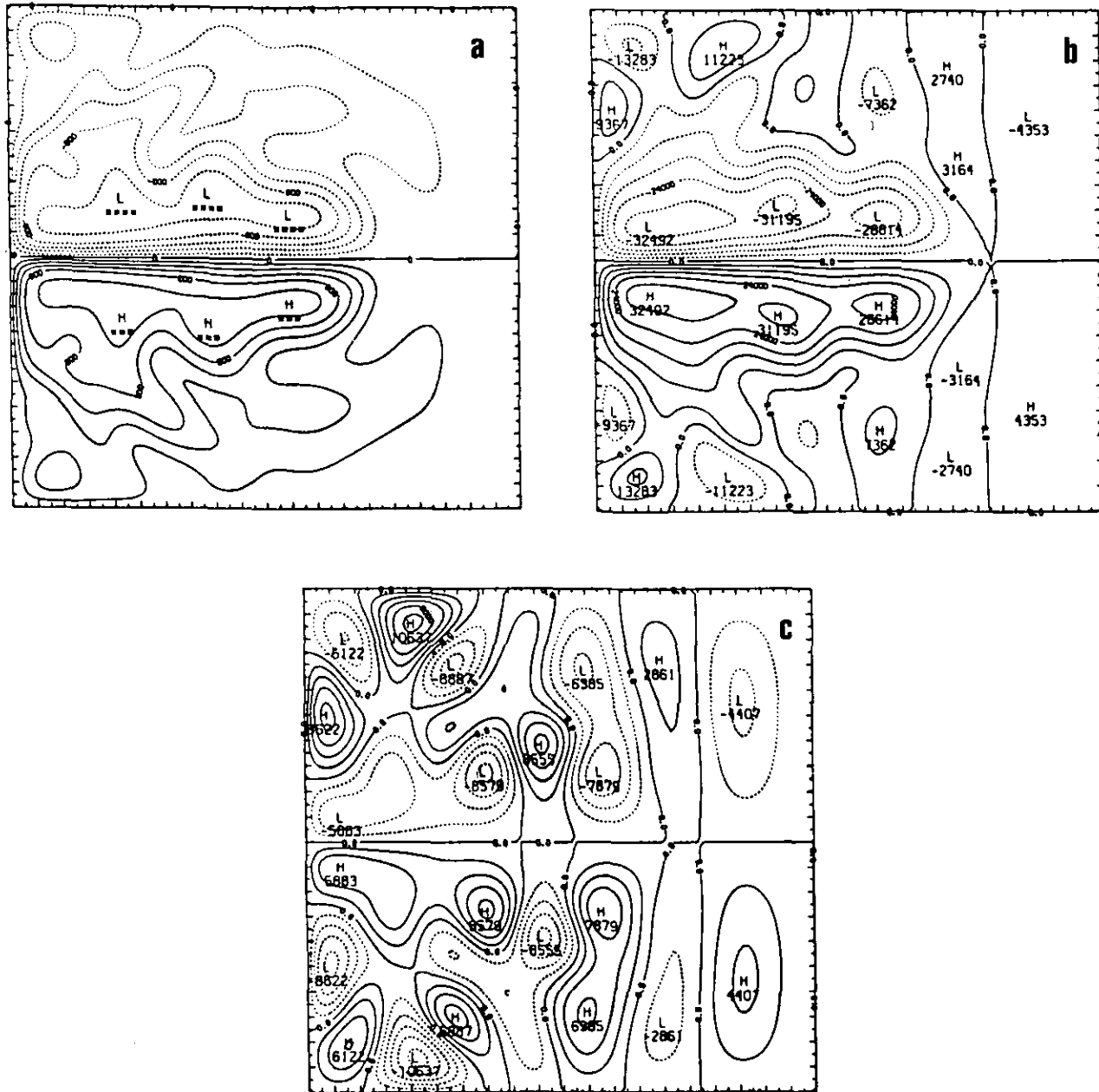
FIG. 4. Typical examples of instantaneous stream functions for layers 1 to 3, at time $t = 2000$ days. Contour intervals (CI) are (a) 20,000 m^2s^{-1} for layer 1, (b) 8000 m^2s^{-1} for layer 2, and (c) 2000 m^2s^{-1} for layer 3. In (a) the major features are the mid-basin eastward jet stream and the westward meandering inner recirculations, superimposed on the double gyre basin scale wind-driven Sverdrup recirculation, which is present in the surface layer only. In the second layer (b), the jet and its inner recirculation is still present, but the absence of Sverdup recirculation makes it possible to clearly observe the Rossby wave patterns radiating from the instabilities of the main flow and propagating westward, as would be seen on short time scale sequences. These Rossby wave patterns are even more visible on the lower layer (c).

The Spinup Phase

During the first period of the spinup (day 0 to 500), corresponding to the setting up of the double-gyre large basin scale circulation, with the build up of the WBC, the two solutions are exactly the same, as can be observed in Figs. 2 and 3. A more quantitative comparison is provided in Figs. 8 and 9, which shows the differences between the kinetic and potential energies, integrated over the whole basin. The similarity between the two runs during this initial phase can clearly be seen: no difference is noticeable in the kinetic energy, while only a very small deficit (a few per

1000) appears after 500 days in the potential energy of the finite difference solution compared with that of the FE solution.

During the second phase (day 500 to 1200), when the flows continue to accelerate in layers 1 and 2, thereby building up the jet which penetrates eastward along the mid-axis of the basin, the two solutions continue to evolve in the same way. The slight deviation already observed on the potential energy integrals becomes stronger but only by up to 1%.

This slight difference must explain why the FE solution becomes destabilized about 15 days before the FD solution,

FIG. 5.   The same as for Fig. 4, but for time $t = 2500$ days. Note that the CI are 1000 m^{2}s^{-1} for layer 3.

the energy level and velocity gradients necessary for the start of shear instabilities being achieved earlier. This can be clearly seen in Fig. 2c, where the kinetic energy in the lower layer starts to increase sooner, and in Figs. 3a and b, where the potential energy decreases in the same time period.

After instabilities in the flow have started, the difference between these integral quantities oscillates. This is logical, since the two solutions have not destabilized at the same time, and thus not exactly at the same initial state. As we are

now in a non-linear regime, even with only slightly different initial conditions, identical solutions cannot be expected. One major point, however, is that, for each integral quantity (potential and kinetic energy), the asymptotic mean value is the same for both simulations. It should be noted, however, that the FE solution on the potential energy integrals is confirmed as being a little more energetic, by a difference of 1 % for the upper interface and by 3 % for the lower interface.
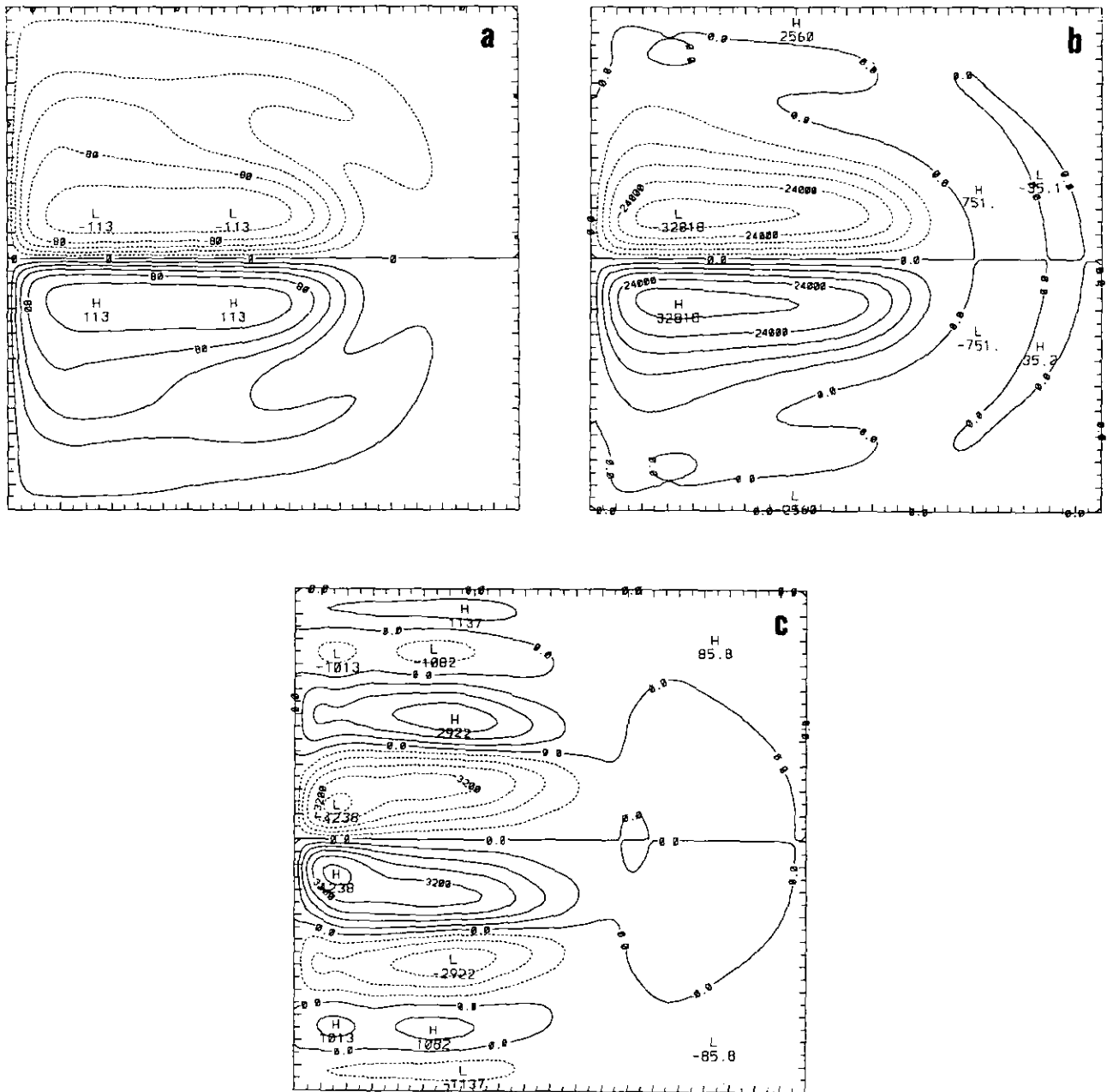

FIG. 6. Finite difference solution. Mean streamfunctions averaged over 1000 days, from day 2000 to day 3000. The CI are (a) 20,000 m²s⁻¹ for layer 1, (b) 6000 m²s⁻¹ for layer 2, and (c) 800 m²s⁻¹ for layer 3.

The Statistically Steady State

Two major conclusions are reached from the comparison of the mean streamfunction fields displayed in Figs. 6 and 7. On the one hand, the main flow characteristics appear to be the same. This is a major point, since it leads to the conclusion that the two models, despite their very different numerical characteristics, result in the same zero-order solution. Consequently, this validates the new FE code.

On the other hand, careful analysis of these solutions reveals that the two mean steady state solutions are not strictly the same. For the upper layers, the FD solution gives higher values, by a few percent, for the eastern half of the basin. For the lower layer, the FE solution displays slightly different patterns for the secondary southernmost and northernmost gyres, which do not extend as far eastward and are more energetic. These differences must certainly be attributed to the grid chosen for the FE model, which appears too coarse over the eastern and extreme southern and northern parts of the basin. Baroclinic motions are thus poorly resolved in these areas.

These similarities between the two solutions confirm the feasibility of using the FE model to resolve the main physical processes of the type of problem we are interested in.
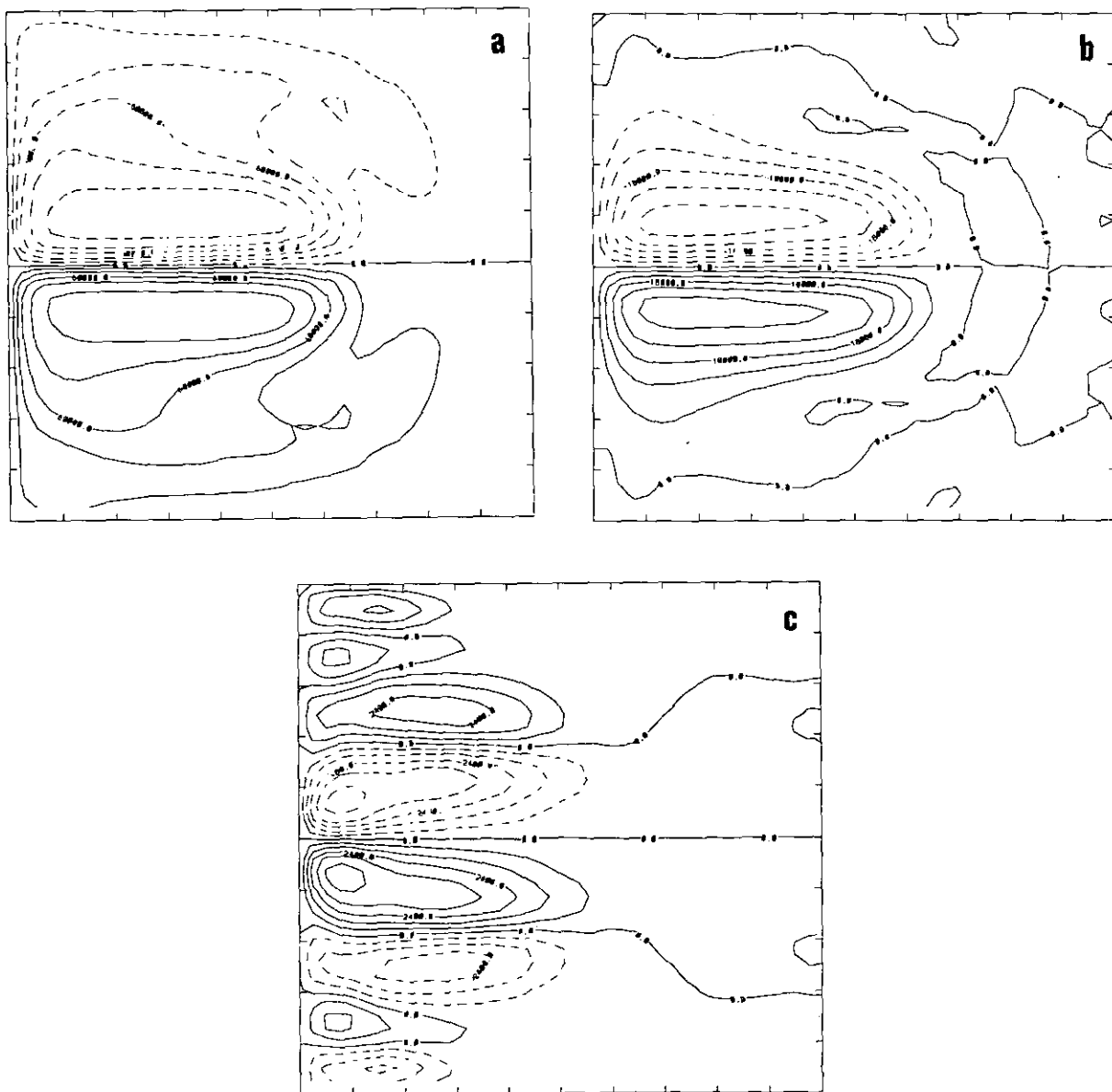

FIG. 7. The same as for Fig. 6, but for the finite element model. The different patterns are qualitatively and quantitatively very similar for the two upper layers. Some differences appear for the lower layer (see comments in Section 5).

However, the small discrepancies observed could provide a warning on the limits concerning the resolution to be used if they are shown to be significant.

Are These Differences Significant?

To answer this question, a third experiment was conducted using the FD model. A very limited amount of noise was introduced in the solution at day 600, that is at the end of the linear regime. A white noise of amplitude of less than $\frac{1}{1000}$ of the maximum streamfunction value in each layer was superimposed on the instantaneous fields, and the experiment was continued up to day 3000, as for the previous simulations.

The conclusions are very instructive:
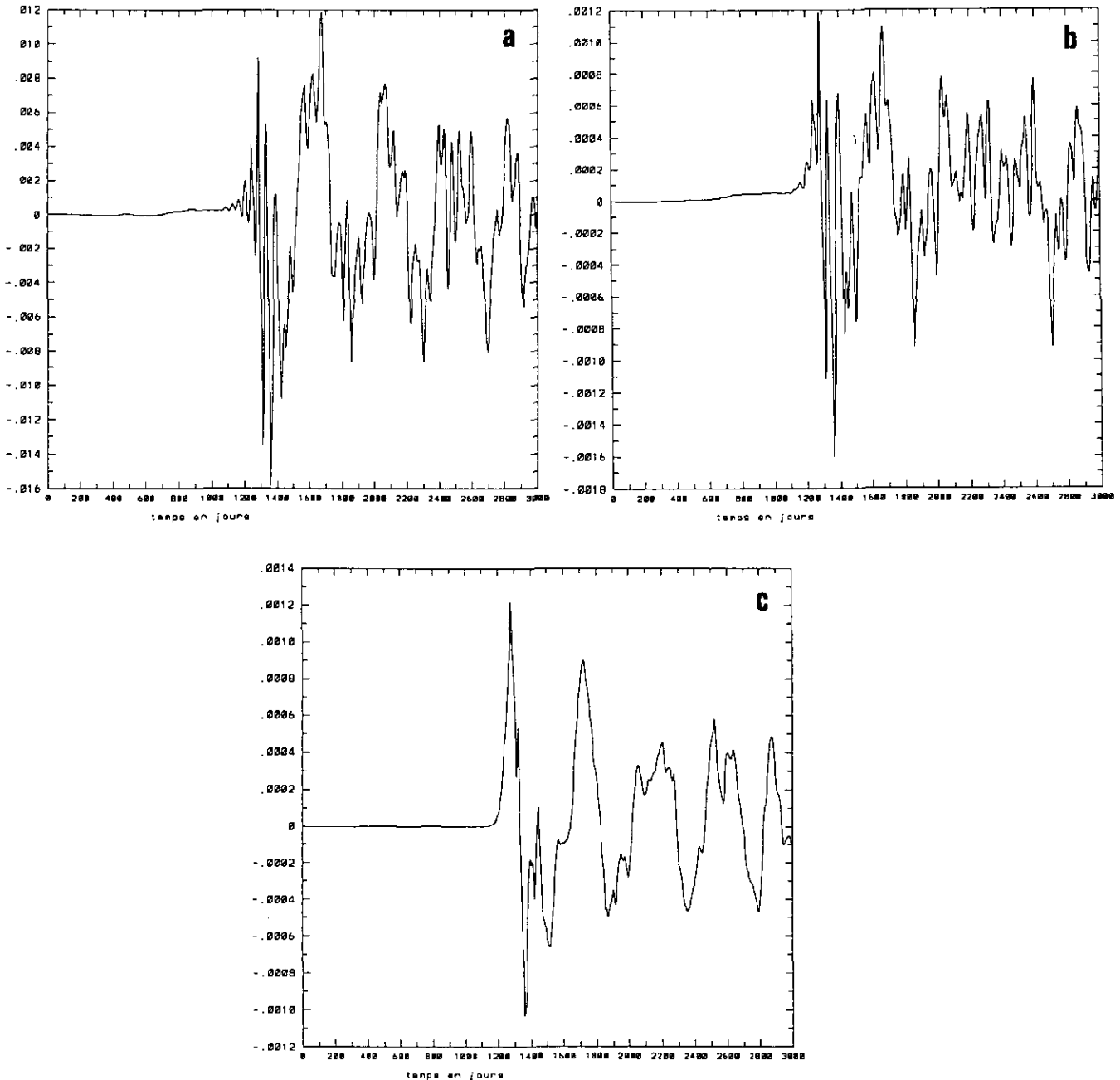
FIG. 8. Time history of the difference between the basin average kinetic energy of the finite element (A) and finite difference (B) solutions over the 3000 days of integration of the comparison test. The units are the same as for Fig. 2. These quantities are the same for the two solutions for layer 1 (a), layer 2 (b), and layer 3 (c), during the first part of the spinup (days 0 to 600), almost the same during the second phase of the jet formation (up to day 1200), and then they start to oscillate, with amplitudes of the order of those for the instabilities (see Fig. 2), and around a mean value which is still near zero. These differences are due to the decorrelation between the instabilities of the two solutions (FD and FE), resulting from the fact that the FE solution reached the unstable regime sooner than the FD solution.

1. The integral kinetic and potential energies computed as above are shown in Fig. 10. It appears that the kinetic energy asymptotic levels remain the same, but the potential energy levels for the perturbed simulation are significantly lower than in the reference simulation. This is particularly true for the upper interface, where there is a difference of 20%.
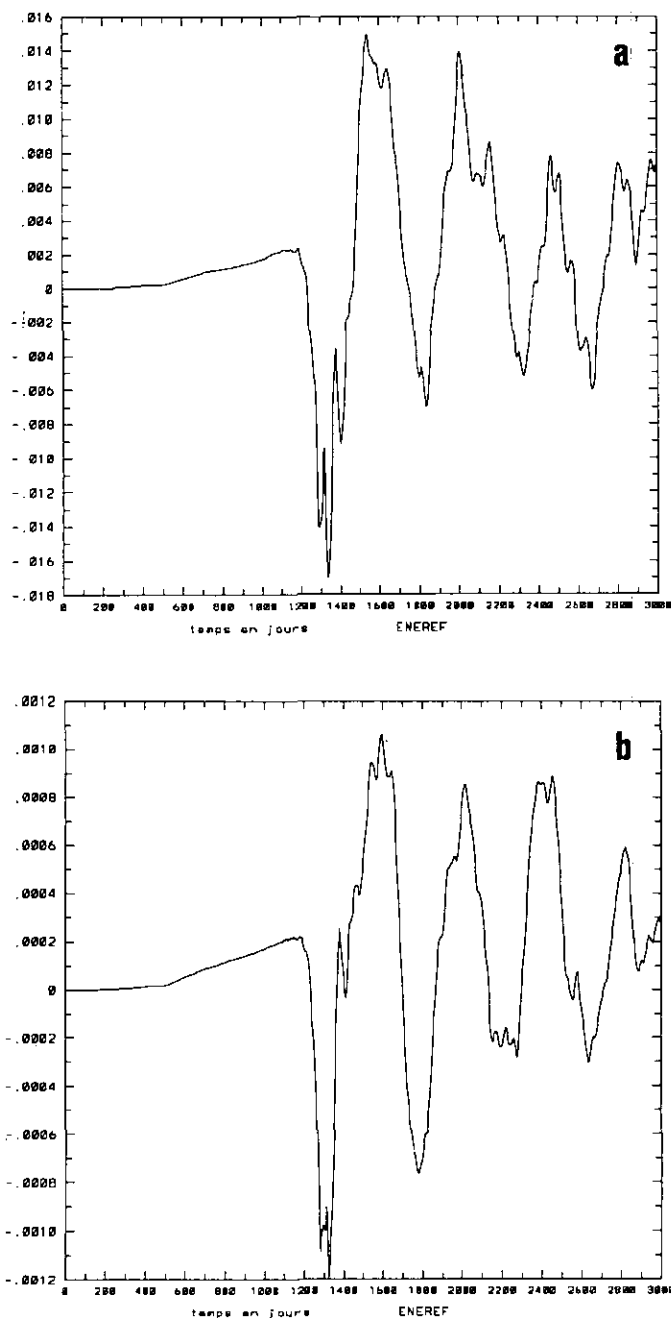

FIG. 9. The same as Fig. 8 but for the potential energy differences. Comments are nearly the same except that the value around which these differences oscillate is not zero: the mean potential energy of the FE solution is slightly higher than that of the FD solution.

2. Destabilization of the flow occurs 60 days earlier for the perturbed experiment, as opposed to the 15 days observed between the FD and FE experiments.

3. Observation of the instantaneous fields (not shown here) reveals a major difference in that the jet itself is destabilized in this new simulation, leading to a decrease in the penetration of the jet, according to a well-known process which has been extensively studied for this class of experiment [28, 1].

These results are a clear indication that the differences noted in the preceding section between the FD and FE simulations can be considered as extremely small: a very small perturbation of the initial conditions leads to much stronger differences than those observed when comparing the FD and FE numerical methods.

CPU and Computer Memory Requirements

Besides examining the feasibility of the new FE method, a major objective of this comparison exercise was to assess the computer time requirements of the two methods. The computations were run on a CRAY-2 computer. As expected, the FE method appears much more costly in terms of CPU time. Basically, per time step and grid point, the cost ratio between FE and FD methods is 40:1. However, given the reduced number of points resulting from the FE grid used for the present test, the final cost per time step at the basin scale is only five times greater for the FE model. It may be noted that these ratios are close to those given earlier by Dumas et al. [18] for their FE model relating to the same QG problem of mid-latitude wind-driven ocean circulations but limited to the barotropic case.

In terms of central memory, the requirement is three times lower for the FE model than for the FD one, due to the fewer integration points required.

6. DISCUSSION AND CONCLUSIONS

The main goals of this paper were: (1) to test the feasibility of using an FEM as an alternative to the FD methods usually developed for high resolution, large-scale ocean circulation modelling; (2) to obtain estimates of the computer cost requirements for the practical application of this alternative method; and (3) to reach some conclusions on the potential interest for ocean modellers of using this class of method, a method which up till now has not been applied to this field of oceanography. The first goal has been dealt with in the previous sections. The conclusion is positive: this method, as implemented here, is able to correctly model the different characteristics of the QG physics of large-scale ocean circulations, their internal mesoscale variability, and the associated nonlinear inverse energy cascade. Two points remain to be discussed: the

a

COMPARISON OF KINETIC ENERGY

COMPARISON OF POTENTIAL ENERGY

b
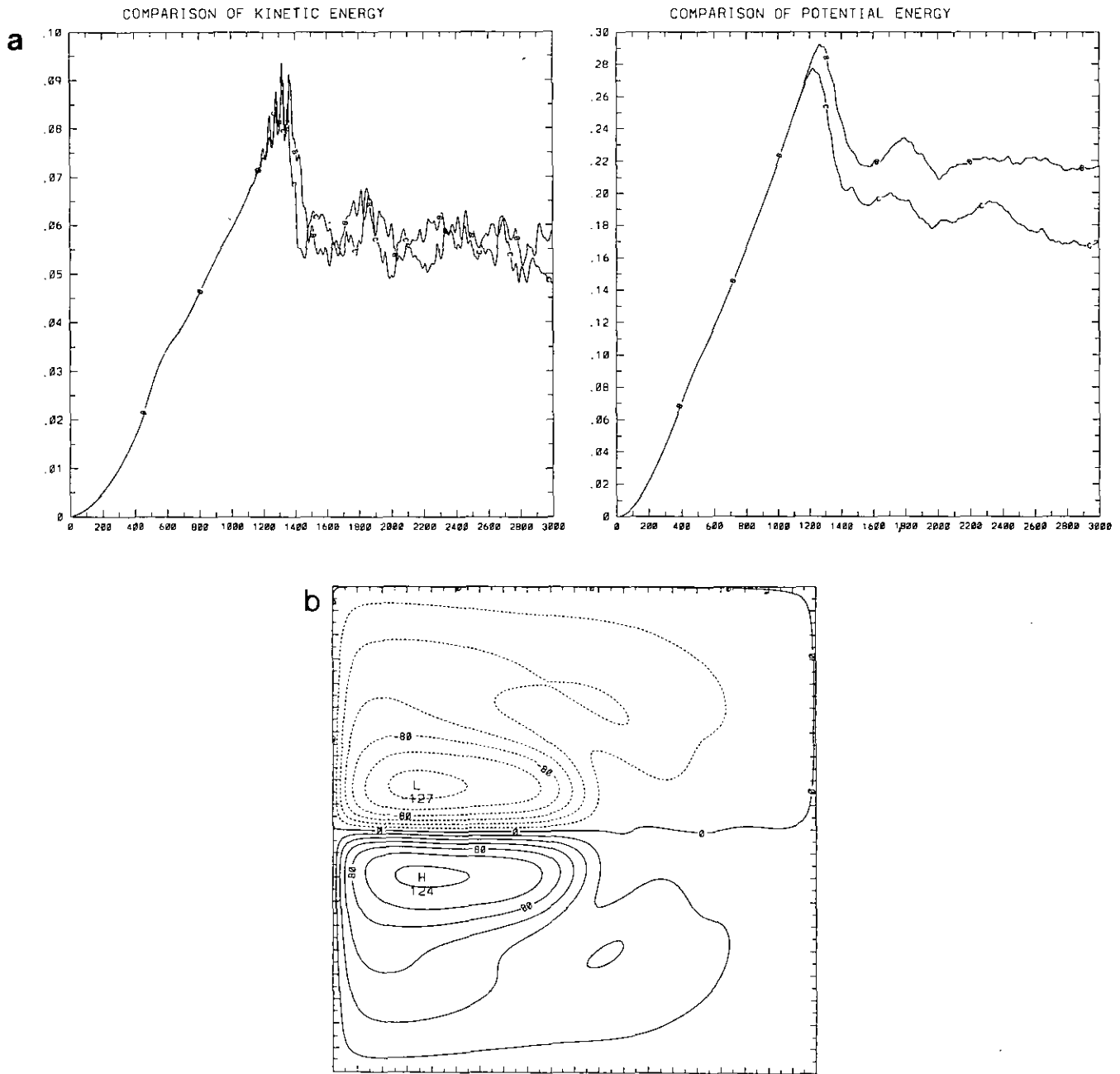
FIG. 10. (a) The same as Figs. 2a and 3a, but for a comparison of the finite difference (B) solution of Fig. 2 with a companion FD experiment (C), where a white noise with an amplitude of less than 1/1000 of the maximum streamfunction value in each layer has been superimposed on the instantaneous fields at day 600, i.e., the end of the quasi-linear regime. One can observe the large difference of about 20% for the mean asymptotic level of potential energy between (B) and (C), to be compared with the very limited difference that is noticeable between the FE (A) and FD (B) solutions displayed on Figs. 2a and 3a. (b) Mean solution in layer 1 for experiment (C), to be compared with Fig. 6a. The major difference is the shortening of the jet penetration, due to its destabilisation.

potential value of the flexibility of the FEM for basin-scale experiments using realistic complex geometries, and the possible extension of the present conclusions, based on a model restricted to the QG physics of ocean circulation, to the more general PE models (PEM) used in dealing with the thermodynamic part of ocean physics.

The test example presented above provides a clear demonstration of the advantage of using the FEM to refine the computation grid in areas where the physical processes need very high resolution. But another major advantage of the FEMs not shown in this paper is the flexibility they offer for matching the computation domain with the complex

shape of real oceanic basins. It was not the aim of this paper to illustrate this flexibility of the FE approach. However, this property of the FEM can be evaluated here in terms of computer costs. It must be remembered that part of the efficiency of the FD code applied to the present benchmarks results from the very fast Helmholtz solver used, but that the application of this solver is limited to rectangular geometries. For practical applications to realistic oceanic domains, the method has to be complemented by a capacitance matrix technique (see, for example, [4]). This extension to real oceanic applications results in extra costs in two ways: (1) an increase of 50% due to the use of a capacitance method which enables the inclusion of real coastlines in the computation, and (2) an extra cost due to the necessity of inserting the integration domain into a rectangular box, thus introducing a lot of new computation points, the number of which is difficult to estimate a priori since it depends on the geometrical characteristics of the study area. For example, for a model of the North Atlantic basin that we are presently developing, the percentage of oceanic points within the rectangular computational domain is 65%, which results in an increase in the basic cost of the simpler FD code by a factor of 2.3.

From the initial cost ratio of 40:1 (per time step and grid point) or 80:1 (when taking into account the fact that the FE time step is half the FD time step), the two above-mentioned characteristics of the FEM—i.e., flexibility on the refinement of the resolution where physically needed and flexibility to fit the integration domain to the complexity of the real geometry of the ocean basins—help to reduce the disadvantages of the FEM in relation to the FDM in terms of computer cost requirements. Overall, this ratio can be reduced in a practical application to a few units (here four), without a loss of accuracy in the resolution of the major physical processes typically involved in the class of problem considered here. However, naturally, it must be recognized that the advantage of an FE model in terms of flexibility to refine the mesh over particular areas would no longer hold if these areas were not a priori known, or varied in time, or if the first Rossby radius of deformation had to be solved everywhere.

The last question to be dealt with relates to whether these conclusions can be extended to the more general PEM needed to incorporate the thermodynamic processes in ocean circulation modelling. Usually, the method of resolution used for this class of model implies splitting the treatment of the barotropic part (vertically integrated) and the baroclinic part of the problem (due to temperature, salinity, and density stratification of the ocean). For the barotropic part, the equation to be solved is of the Poisson type, as used above for the barotropic mode of the QG model considered in this paper. For this part of the PEM resolution, the previous conclusions are thus valid. What remains to be investigated is the way the resolution of the baroclinic part

of the problem has to be implemented in a PE FE model and what differences arise in relation to models based on the classical FDM. To answer these questions, such a PE FE model needs to be developed, but this is beyond the scope of the present paper. However, it may already be concluded that FEMs, besides their value in QG modelling, may also a priori be applied in the fields of PE ocean circulation modelling.

REFERENCES

1. B. Barnier, B. L. Hua, and C. Le Provost, *J. Phys. Oceanogr.* **21**, 976 (1991).
2. C. Bernier, Ph.d. thesis, Institut National Polytechnique de Grenoble, 1990 (unpublished).
3. G. Birshoff, Regional Conf. Series in Applied Math., Vol. 11 (SIAM, Philadelphia, 1972).
4. E. Blayo and C. Le Provost, *J. Comput. Phys.* **104**, 347 (1993).
5. R. Bleck and D. B. Boudra, *J. Phys. Oceanogr.* **11**, 755 (1981).
6. R. Bleck, H. P. Hanson, D. Hu, and E. B. Kraus, *J. Phys. Oceanogr.* **19**, 1417 (1989).
7. A. F. Blumberg and G. L. Mellor, in *3-D Coastal Ocean Models*, edited by N. Heaps (AGU, Washington, DC, 1987).
8. C. W. Böning, *Dyn. Atmos. Oceans* **10**, 63 (1986).
9. C. W. Böning, R. Döscher, and R. G. Budich, *J. Phys. Oceanogr.* **21**, 1271 (1991).
10. F. O. Bryan and W. R. Holland, in *Spec. Pub. Inst. of Geophys.* (Univ. of Hawaï, Honolulu, 1989).
11. K. Bryan and M. C. Cox, *Tellus* **19**, 54 (1967).
12. K. Bryan, *J. Comput. Phys.* **3**, 347 (1969).
13. K. Bryan, S. Manabe, and R. C. Pacanowski, *J. Phys. Oceanogr.* **5**, 30 (1975).
14. J. J. Connor and J. D. Wang, in *Numerical Methods in Fluid Dynamics* (Pentech, London, 1974).
15. M. D. Cox, *Deep Sea Res.* **17**, 45 (1970).
16. M. D. Cox, in *Proc. Symposium on Numerical Models of Ocean Circulation, Durhan, NH* (Nat. Acad. Sciences, Washington, DC, 1975).
17. A. M. Davies, *Progress in Oceanogr.* **15**, 72 (1985).
18. E. Dumas, C. Le Provost, and A. Poncet, in *4th Int. Conf. on Finite Elements in Water Resources, Hanover* (Springer-Verlag, New York/Berlin, 1982).
19. G. J. Fix, *SIAM J. Appl. Math.* **29**, 371 (1975).
20. G. R. Flierl, *Dyn. Atmos. Oceans* **2**, 341 (1978).
21. H. Friedrich, *Proc. Symp. Maths-Hydrodyn. Invest. Phys. Processes in the sea 10, 1967*, p. 134.
22. P. R. Gent and J. C. McWilliams, *Dyn. Atmos. Oceans* **7**, 67 (1983).
23. G. Grotkop, *Comput. Methods Appl. Mech. Eng.* **2**, 147 (1973).
24. D. B. Haidvogel, A. R. Robinson, and E. F. Schulman, *J. Comput. Phys.* **34**, 1 (1980).
25. D. B. Haidvogel, J. L. Wilkin, and R. Young, *J. Comput. Phys.* **94**, 151 (1991).
26. W. R. Holland and L. B. Lin, *J. Phys. Oceanogr.* **5**, 642 (1975).
27. W. R. Holland, *J. Phys. Oceanogr.* **8**, 363 (1978).
28. W. J. Holland and W. J. Schmitz, *J. Phys. Oceanogr.* **15**, 1859 (1985).
29. A. Kasahara, *Mon. Weather Rev.* **102**, 504 (1974).
30. C. Le Provost, in *Finite Element in Water Resources* (Springer-Verlag, New York/Berlin, 1984).

31. C. Le Provost and P. Vincent, *J. Comput. Phys.* **65**, 273 (1986).

32. C. Le Provost and J. Verron, *Dyn. Atmos. Oceans* **11**, 175 (1987).

33. M. J. Lighthill, *Phil. Trans. R. Soc. London* **265**, 45 (1969).

34. J. P. Mc Creary, *Phil. Trans. R. Soc. London* **302**, 385 (1981).

35. R. N. Miller, A. R. Robinson, and D. B. Haidvogel, *J. Comput. Phys.* **50**, 38 (1983).

36. A. L. New, R. Bleck, Y. Jia, R. Marsh, M. Huddleston, and S. Barnard, James Rennell Centre for Ocean Circulation Report, 1992.

37. J. M. Oberhuber, in *Advanced Physical Oceanography Numerical Modelling* (Reidel, Dordrecht, 1986), p. 511.

38. J. M. Oberhuber, *J. Phys. Oceanogr.* in press, (1993).

39. J. J. O'Brien and R. O. Reid, *J. Atmos. Sci.* **24**, 197 (1967).

40. N. A. Phillips, *Q. J. Roy. Meteorol. Soc.* **82**, 123 (1956).

41. R. T. Pollard, *Deep Sea Res.* **17**, 812 (1970).

42. A. R. Robinson and L. J. Walstad, *J. Appl. Math.* **3**, 89 (1987).

43. A. S. Sarkisyan, *Okeanologie* **11**, 393 (1962).

44. P. Schopf and M. A. Cane, *J. Phys. Oceanogr.* **13**, 917 (1983).

45. A. J. Semtner and R. M. Servin, *J. Geophys. Res.* **97**, 5493 (1992).

46. C. Taylor and J. M. Davies, in *Finite Elements in Fluids* (Wiley, New York, 1975).

47. D. Van Forest and G. B. Brundrit, in *Advanced Physical Oceanography Numerical Modelling* (Reidel, Dordrecht, 1986), p. 523.

48. D. J. Webb, P. D. Killworth, A. C. Coward, and S. R. Thompson, *Natural Environment Council*, Swindon, UK, 1991.

49. J. J. Westerink and W. G. Gray, *Rev. Geophys.* **29**, 210 (1991).